

## RESEARCH ARTICLE

10.1002/2015JD024035

## Key Points:

- SP-CCSM4 captures the mechanisms explaining the EASM intraseasonal variability
- The mean state and annual cycle of the EASM are better simulated by SP-CCSM4 than CCSM4
- The faster northward propagation of ISO in SP-CCSM4 may be related to the dry condition over West Pacific Warm Pool

## Correspondence to:

Y. Jin,  
yjjin7@masonlive.gmu.edu

## Citation:

Jin, Y., and C. Stan (2016), Simulation of East Asian Summer Monsoon (EASM) in SP-CCSM4: Part I—Seasonal mean state and intraseasonal variability, *J. Geophys. Res. Atmos.*, 121, 7801–7818, doi:10.1002/2015JD024035.

Received 3 AUG 2015

Accepted 15 APR 2016

Accepted article online 20 APR 2016

Published online 12 JUL 2016

## Simulation of East Asian Summer Monsoon (EASM) in SP-CCSM4: Part I—Seasonal mean state and intraseasonal variability

Yan Jin<sup>1</sup> and Cristiana Stan<sup>1,2</sup>

<sup>1</sup>Department of Atmospheric, Oceanic, and Earth Sciences, George Mason University, Fairfax, Virginia, USA, <sup>2</sup>Center for Ocean-Land-Atmosphere Studies, Fairfax, Virginia, USA

**Abstract** The mean state and intraseasonal variability of the East Asian Summer Monsoon (EASM) simulated by the Super-Parameterized Community Climate System Model version 4 (SP-CCSM4) and the conventionally parameterized CCSM4 are evaluated against observations. The SP-CCSM4 model has a better simulation of the May-June-July-August seasonal mean state of EASM than CCSM4, although it produces a dry bias over the EASM area compared to observations. The dry bias in SP-CCSM4 is associated with the erroneous northward displacement of the western North Pacific subtropical high. The SP-CCSM4 model simulates the reasonable monsoon onset and northward propagation of the monsoonal precipitation, yet the rainband marches faster and reaches to a higher latitude than in observations. The mechanisms associated with the northward propagation of the intraseasonal oscillation (ISO) of EASM are also captured by SP-CCSM4. The cyclonic vorticity and the moisture convergence lead the convective activity, favoring the northward propagation of convection. The easterly wind shear and air-sea interaction mechanisms in the model are realistic and show contributions to the northward propagation of the ISO of the model. The SP-CCSM4 model captures many facets of the stepwise northward propagation of the precipitation belt in the EASM region, including the Mei-yu season. However, compared to the observations, in the model the onset of the Mei-yu season takes place 5 days earlier and the duration of the Mei-yu's rainy episode is shorter. The CCSM4 model has large deficiencies in simulating the intraseasonal variability of EASM.

### 1. Introduction

The East Asian Summer Monsoon (EASM) is an important subsystem of the boreal summer Asian-Pacific monsoon system. The earliest onset of the boreal summer monsoon system occurs at the end of April or early May and is characterized by an abrupt increase of precipitation in the central and southern Indo-China Peninsula. By mid-May the precipitation extends to the South China Sea (SCS), triggering the breakout of the monsoon over the SCS region. After the onset, the Asian-Pacific monsoon evolves into two systems: one system propagates northwestward to India, leading to the onset of the Indian Summer Monsoon (ISM), and the other propagates northward and northeastward to East Asia, leading to the EASM [Ding and Chan, 2005; Ding et al., 2005; He, 2009; He et al., 2007].

The domain of the EASM varies from study to study. Sometimes it only covers subtropical East Asia [Ding and Chan, 2005; Wang et al., 2005], whereas other times it includes the SCS [Ding, 1992]. In this study we adopt the domain which covers both subtropical East Asia and SCS (110°E–120°E, 10°N–45°N) to emphasize the hybrid subtropical-tropical characteristics of EASM.

One of the main characteristics of the EASM in subtropical East Asia is known as the Mei-yu/Baiu, which represents a unique rainy episode in the EASM seasonal march [Ding and Chan, 2005; Ding et al., 2005]. In different regions different terminologies have been used to denote this seasonal rain belt. In China, the Mei-yu season is usually referred to as the rainy episode over the Yangtze River Valley from mid-June to mid-July [Ding et al., 2005; Tao and Chen, 1987], and this definition is adopted in this paper.

The strength, shape, and position of the western North Pacific subtropical high (WNPSH) influence the precipitation of the EASM system [Lu and Dong, 2001; Mao et al., 2010]. The WNPSH links the tropical and extra-tropical circulations [Sun and Ying, 1999], and the low-level jet at the northwestern edge of WNPSH transports large amounts of moisture to the region to its north [Lu, 2001; Lu and Dong, 2001; Lu et al., 2008; Zhang et al., 2009]. Also, the meridional shifts of WNPSH have been observed to be associated with

the onset and retreat of the EASM [He et al., 2001; Lu and Dong, 2001; Yang and Sun, 2003; Zhang and Tao, 1999; Zhou et al., 2009].

The EASM is also characterized by the intraseasonal variability (ISV) of the boreal summer Asian-Pacific monsoon system, and the northward propagating intraseasonal oscillation (NPISO) dominates the ISV of EASM [Huang et al., 2003]. The mechanisms proposed to explain the formation and propagation of NPISO are attributed to the atmospheric internal dynamics [Drbohlav and Wang, 2005; Jiang et al., 2004; Wang et al., 2009] and to external influences [Hsu and Weng, 2001; Kemball-Cook and Wang, 2001; Mao et al., 2010; Tsou et al., 2005; Wang et al., 2009, 2000; Wang and Zhang, 2002; Zhang et al., 2009].

Wang et al. [2009] divided the air-sea interaction theories into two categories: the propagating air-sea interaction theory and the stationary air-sea interaction theory. In both theories, a warm sea surface temperature (SST) anomaly leading the convective activity favors the propagation of convection. The propagating air-sea interaction theory was initially developed for explaining the NPISO in the Indian Ocean (IO) [Kemball-Cook and Wang, 2001] and later extended to the northward propagation of boreal summer ISO over WNP and SCS [Hsu and Weng, 2001; Wang et al., 2009]. The heating associated with the convection over the equatorial eastern IO induces convectively coupled Kelvin and Rossby waves. Both waves act to decrease the southwesterly flow in the northern Tropics, thus reducing the latent heat loss and warming up the northern IO. At the same time, the small cloud cover to the north of convection allows the downward solar radiation to warm up the surface and destabilize the low-level atmosphere, thus favoring the northward propagation of ISO.

The stationary air-sea interaction supports the ISO by providing a restoring mechanism of the summer monsoon trough over SCS when perturbed by a high-pressure ISO anomaly. Wang and Zhang [2002] defined this restoring mechanism as the collective effects of two thermodynamic feedback: SST-cloud/radiation and SST-wind/evaporation, which turn the high-pressure anomaly into a low-pressure anomaly.

The atmospheric internal dynamics include the vertical shear mechanism and the boundary layer moisture-convection feedback mechanism [Drbohlav and Wang, 2005; Jiang et al., 2004; Wang et al., 2009]. The process associated with the vertical shear mechanism is the generation of positive (negative) barotropic vorticity to the north (south) of the convection developing in a region dominated by vertical easterly wind shear. The barotropic vorticity aloft triggers the moisture convergence in the boundary layer to the north of the convection due to Ekman pumping and favors the northward propagation of convection. In the moisture-convection feedback mechanism the northward propagation of the convection is favored by the meridional gradient of specific humidity.

The mechanisms mentioned above pose numerous challenges for numerical models, and most of the atmosphere-ocean general circulation models (AOGCMs) do not accurately simulate the spatial and/or intraseasonal variation of the monsoon precipitation [Randall et al., 2007]. Rajendran et al. [2004] analyzed the summer monsoon over South Asia, East Asia, and WNP in the Meteorological Research Institute Coupled General Circulation Model version 2. This model simulates many of the observed features of the South Asian and WNP summer monsoon except for the EASM. The model underestimates the precipitation over Southeast China and simulates an earlier onset of EASM along with an earlier occurrence of the rainfall over Southeast China. In addition, the model fails to simulate the northward propagation of the rain belt over Southeast China. Kusunoki and Arakawa [2012] evaluated the June-July mean precipitation of EASM simulated by the models in the Coupled Model Intercomparison Project 3 (CMIP3) and found that most models underestimate the precipitation climatology and precipitation intensity over the East Asian region (110°E–150°E, 20°N–50°N).

Previous modeling studies have identified the horizontal resolution and the representation of convection as the main causes of these model biases. Sperber et al. [2012] noted that the multimodel mean of the Coupled Model Intercomparison Project 5 (CMIP5) models has a better simulation of seasonal mean precipitation, large-scale circulation, and boreal summer ISO than the CMIP3 multimodel mean. They attributed the improvements to the higher resolution of CMIP5 than CMIP3 models and different convective parameterizations. However, CMIP5 models still underestimate precipitation in the rainy season [Kusunoki and Arakawa, 2015], and Sperber et al. [2013] attribute the error to the weaker than observed cross-equatorial flow in the models. Zhou and Li [2002] used a resolution-varying atmospheric GCM with a local zoom centered on China, where the resolution was 1.5° (longitude) × 1° (latitude). The model captures the main characteristics of EASM such as the large-scale monsoon airflows and the cross-equatorial southwesterly flow, but is unable

to simulate most of the characteristics of the monsoonal precipitation. The observed heavy rain belt along the Yangtze River Valley is missed in the simulation because the model produces a weaker than observed WNPSH and land-sea thermal contrast. *Chen et al.* [2010] analyzed the ability of Community Atmospheric Model version 3.5 (CAM3.5) to simulate the EASM and the sensitivity of the simulation to changes in the convection scheme. The simulation of the seasonal mean precipitation of EASM shows some improvements, but the magnitude of rainfall remains smaller than observed over the tropical and subtropical regions. Additionally, the seasonal march of precipitation does not improve with the changes in the parameterization of convective processes. For example, the subtropical rain belt is located at a higher latitude, the onset of the Mei-yu season begins 3 months earlier than in the observations, and the precipitation is overestimated and lasts longer in the northern part of the EASM region. The authors find that none of the changes in the parameterization of convection improves the simulation of the meridional monsoon circulation in the EASM region, which can be a source of error for the precipitation simulation.

This paper is part I of a two-part study of the EASM using SP-CCSM4. The current study is focused on evaluating the ability of a model with explicit representation of cloud processes, SP-CCSM4, to simulate the EASM, including its mean state and the mechanisms associated with the northward propagation of EASM ISO. Previous studies using the superparameterization [*Khairoutdinov and Randall*, 2001; *Grabowski*, 2001] showed that the multiscale representation of cloud properties improves the simulation of ISM and the northward propagation of Boreal Summer Intraseasonal Oscillation [*DeMott et al.*, 2013]. The impact of superparameterization on the simulation of EASM is unknown. The relative importance of superparameterization over the conventional convective parameterization in the simulation of EASM is not understood.

The remaining of the paper is organized as follows: Section 2 provides a description of the model, data, and the analytical methods used in the paper. The comparison among observations, SP-CCSM4, and CCSM4 is discussed in section 3, including the comparison of seasonal mean state and ISO of EASM. Finally, a summary of the main results and discussions are presented in section 4.

## 2. Model, Data, and Method Description

### 2.1. Model Description

The models used in this study are the Super-Parameterized Community Climate System Model version 4 (SP-CCSM4) and the conventionally parameterized version CCSM4 [*Gent et al.*, 2011]. The SP-CCSM4 model uses an explicit 2-D cloud resolving model (CRM) embedded in each GCM grid column [*Huffman et al.*, 1997; *Stan and Xu*, 2014]. The CRMs are aligned in the east-west direction, have a horizontal resolution of 4 km, and 30 levels in the vertical. The simulations analyzed in this paper were carried out at the horizontal resolution for the atmospheric model of  $2.5^\circ$  (longitude)  $\times$   $1.9^\circ$  (latitude) using a finite volume representation of the dynamical core. The resolution of the ocean model is  $1^\circ \times 1^\circ$  in the horizontal. The sea ice model uses the same resolution as the ocean model, and the horizontal resolution in the land model is the same as in the atmosphere model. The simulations are initialized in January 2006, span 100 years, and are driven by a constant external forcing. In this paper the data between 2071 and 2100 were used for evaluating the simulation of the EASM.

### 2.2. Data

The verification data used in this paper consist of the following: (1) monthly and pentad precipitation from the Global Precipitation Climatology Project [*Huffman et al.*, 1997]. The precipitation data cover the period between 1983 and 2012, with  $2.5^\circ \times 2.5^\circ$  spatial resolution. (2) Monthly and daily 2-D and 3-D atmospheric variables from the National Centers for Environmental Prediction (NCEP) reanalysis [*Kalnay et al.*, 1996]. The horizontal resolution of the 3-D data is  $2.5^\circ \times 2.5^\circ$ , and vertically, there are 17 levels. The 2-D data have approximately  $1.9^\circ \times 1.9^\circ$  spatial resolution. (3) The European Center for Medium-Range Weather Forecasts Reanalysis-Interim (ERA-Interim) [*Dee et al.*, 2011]. Both 3-D and 2-D data have approximately  $0.703^\circ \times 0.703^\circ$  spatial resolution, and vertically, there are 37 levels for 3-D data. The 3-D atmospheric variables include geopotential height (GPH), wind, specific humidity, and temperature, while the 2-D fields contain surface temperature, sensible heat flux, and latent heat flux. The ERA-Interim monthly data are for 1983–2012, while the daily data are from 1979 to 2006. (4) Daily mean outgoing longwave radiation (OLR) data from National Oceanic and Atmospheric Administration (NOAA) [*Liebmann and Smith*, 1996]. The grid spacing of OLR is  $2.5^\circ \times 2.5^\circ$  (longitude  $\times$  latitude), and the time period spans from 1979 to 2006. (5) Daily

SST data from NOAA Optimum Interpolation daily  $0.25^\circ$  SST [Reynolds *et al.*, 2002] from 1982 to 2006. All data sets used in the analyses, including the model output, are interpolated from their original grid to the  $2.5^\circ \times 2.5^\circ$  horizontal resolution.

### 2.3. Method

The May-June-July-August (MJJA) climatological means were computed for observations, SP-CCSM4, and CCSM4 using monthly data. The SP-CCSM4 and CCSM4 models' ability to simulate the observed patterns of the climatological means is measured by the difference between each of the models and observations, referred to as biases, and by the centered pattern correlation (spatial mean removed). The annual cycle of the EASM was evaluated by constructing pentad means from daily averages and taking the zonal mean between  $110^\circ\text{E}$ – $120^\circ\text{E}$ . The differences of annual cycle between observations and each of the models are also presented.

The evolution of the intraseasonal variability of EASM was evaluated in the composite analysis [Hsu and Weng, 2001; Tsou *et al.*, 2005] of 30–60 day bandfiltered data for observations and each of the models. Since the northward propagation of EASM occurs mostly during May through July, the composite analysis is based on May, June, and July (MJJ). The composite analysis of the EASM life cycle follows the method of [Kemball-Cook and Wang, 2001]. Before doing the composite analysis the intraseasonal oscillation was extracted. First, the daily anomalies were computed by removing the mean annual cycle (mean plus the first three harmonics) from the daily data. Then the intraseasonal variability was retained by applying a 30–60 day band filtering to the daily anomalies. The life cycle of an event was constructed based on an OLR index. This OLR index was constructed by taking the area average of the 30–60 day bandfiltered OLR anomaly over SCS ( $112.5^\circ\text{E}$ – $120^\circ\text{E}$ ,  $10^\circ\text{N}$ – $17.5^\circ\text{N}$ ), where the 30–60 day bandfiltered OLR variance is maximum in the observations (Figure 10a). This region is unchanged when calculating the OLR index for SP-CCSM4 and CCSM4. Day 0 of the cycle is centered on the day when the OLR index during MJJ is less than minus 1 standard deviation ( $-13.18 \text{ W/m}^2$ ) over SCS. The life cycle of an EASM event consists of 12 phases starting from 15 days before and proceeding 40 days after Day 0. In observations we identified 36 events from 1979 to 2006, whereas the SP-CCSM4 produced 53 events and CCSM4 produced 30 events during the 30 years used in the analysis. The statistical significance of the composite is assessed using the Student's *t* test.

## 3. Model Biases

This section evaluates the models' skill in simulating the seasonal mean state, annual cycle, and intraseasonal variability. The mean state includes precipitation, the large-scale monsoon airflows, meridional circulation, surface temperature, and surface heat fluxes. Because EASM is characterized by a northward propagation of the precipitation, the annual cycle of the zonal mean precipitation and WNPSH index is compared between each of the models and observation. Both the NCEP and ERA-Interim data sets were used as observations for the comparison, and they produced similar results. For this reason, only the comparison between the models and ERA-Interim is shown.

### 3.1. Seasonal Mean of EASM

Table 1 lists the pattern correlation coefficients between each of the two models and observations for MJJA mean of different variables. Sperber *et al.* [2013] used the pattern correlation to evaluate the CMIP3 and CMIP5 model skill in simulating the mean state of EASM. Generally, SP-CCSM4 has higher correlation than CCSM4, and the largest difference between the two models occurs in the field of precipitation, 850 hPa wind, meridional circulation, and vertically integrated moisture transport.

Figure 1 shows the MJJA mean precipitation in observation and model biases, defined as the difference between the values simulated by the model and the observed values. Both models underestimate the magnitude of precipitation over Southeast China, Korean Peninsula, and the region south of Japan, indicating a weak subtropical monsoon trough in the models. The precipitation deficiency in CCSM4 is more intense and extends to SCS (Figure 1c). SP-CCSM4 simulates excessive precipitation over WNP (Figure 1b), indicating a northward displacement of the tropical monsoon trough (figure not shown). In CCSM4 the region with excessive precipitation is located over the central China (figure not shown). The pattern correlation of MJJA mean precipitation is higher in SP-CCSM4 than in CCSM4 (Table 1), which means the spatial distribution of mean precipitation is better simulated in SP-CCSM4. The area average of the model bias is smaller in SP-CCSM4,

**Table 1.** Pattern Correlation Coefficients of MJJA Mean State Between Models and Observations<sup>a</sup>

Variables		SP-CCSM4	CCSM4
Precipitation		<b>0.629</b>	0.238
850 hPa GPH		0.824	<b>0.839</b>
850 hPa wind	Magnitude	<b>0.654</b>	0.338
	U component	<b>0.638</b>	0.618
	V component	<b>0.583</b>	0.402
200 hPa wind	Magnitude	0.895	<b>0.933</b>
	U component	0.943	<b>0.960</b>
	V component	<b>0.689</b>	0.308
Meridional circulation	V component	<b>0.933</b>	0.879
	Omega component	<b>0.859</b>	0.213
Vertically integrated moisture transport	Magnitude	0.516	<b>0.617</b>
	U component	<b>0.729</b>	0.370
	V component	<b>0.720</b>	0.626
Latent heat flux		<b>0.909</b>	0.771
Sensible heat flux		<b>0.969</b>	0.792

<sup>a</sup>The domain of each field is consistent with the spatial pattern of the mean state in Figures 4–6. The domain is 110°E–150°E, 10°N–50°N for precipitation, 850 hPa and 200 hPa wind fields, vertically integrated moisture transport, surface temperature, and latent and sensible heat fluxes. The domain is 105°E–180°E, 10°N–50°N for 850 hPa GPH and 110°E–120°E, 10°N–50°N; 1000–100 hPa for meridional circulation. The model with the higher spatial pattern correlation coefficient is highlighted.

and the visual inspection of Figures 1b and 1c may suggest that in SP-CCSM4 the smaller value results from the cancelation of errors between the northern and southern parts of the domain. The mean value of the precipitation bias for the region between 20°N–50°N in SP-CCSM4 is –0.45 mm/d and –1.61 mm/d in CCSM4. The evaluation of the two models with respect to the root-mean-square error (RMSE) reveals that SP-CCSM4 (1.30 mm/d) has a larger value than CCSM4 (0.88 mm/d). Since by definition RMSEs weigh more the errors with larger absolute values than the errors with smaller absolute values [e.g., Willmott and Matsuura, 2005; Chai and Draxler, 2014] one can speculate that RMSE in SP-CCSM4 is dominated by the outliers. The outlier may be related to one of the limitations of the multiscale framework, namely, the two-dimensional geometry and periodicity of the CRM domain. Past CRM studies [e.g., Tompkins, 2000; Zeng et al., 2007; Wang and Sobel, 2011] have indicated that 2-D convection may exhibit excessive high-frequency variability. In some instances, the domain configuration may artificially amplify strong convective events.

Following Lu et al. [2008], the GPH at 850 hPa is adopted to describe the WNPSH characteristics. Figure 2a shows the isopleth of 1500 m (solid contours) and the ridge line (dashed lines) of WNPSH in observation (black), SP-CCSM4 (red), and CCSM4 (blue). The model biases for the 1500 m isopleth are shown in

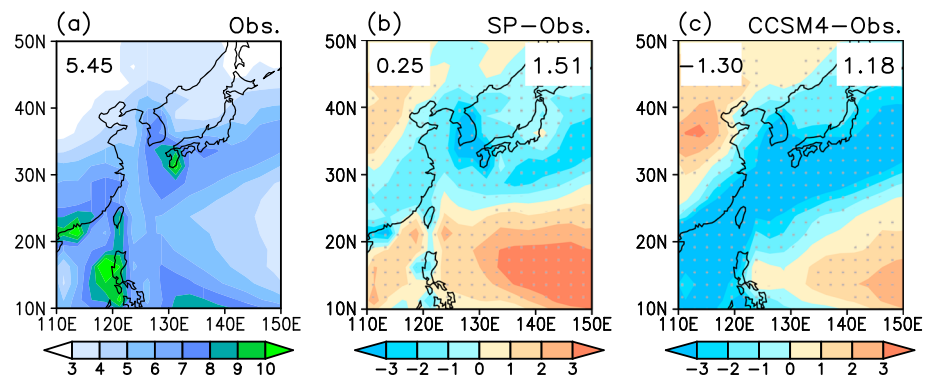


**Figure 1.** MJJA mean precipitation rate (unit: mm/d). (a) Observation, (b) the difference between SP-CCSM4 and observation, and (c) the difference between CCSM4 and observation. The dots in Figures 1b and 1c denote the regions exceeding 95% significance level. The value at the top-left corner denotes the domain-averaged mean precipitation in observation (Figure 1a) and the domain-averaged precipitation difference between model and observation (Figures 1b and 1c). The value at the top-right corner of Figures 1b and 1c denotes the domain-averaged root mean square of precipitation difference between model and observation.

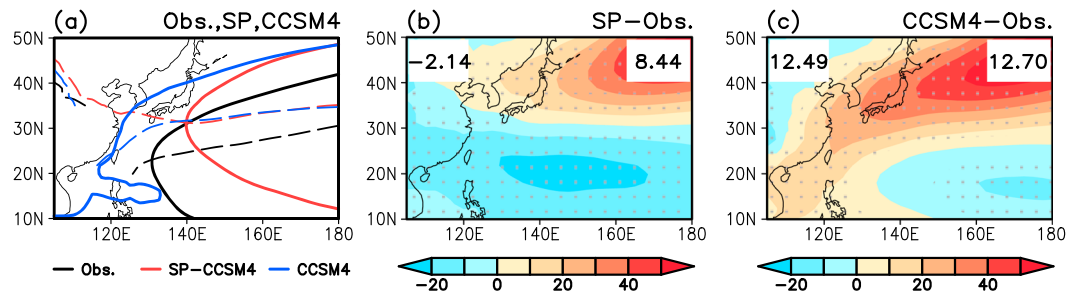
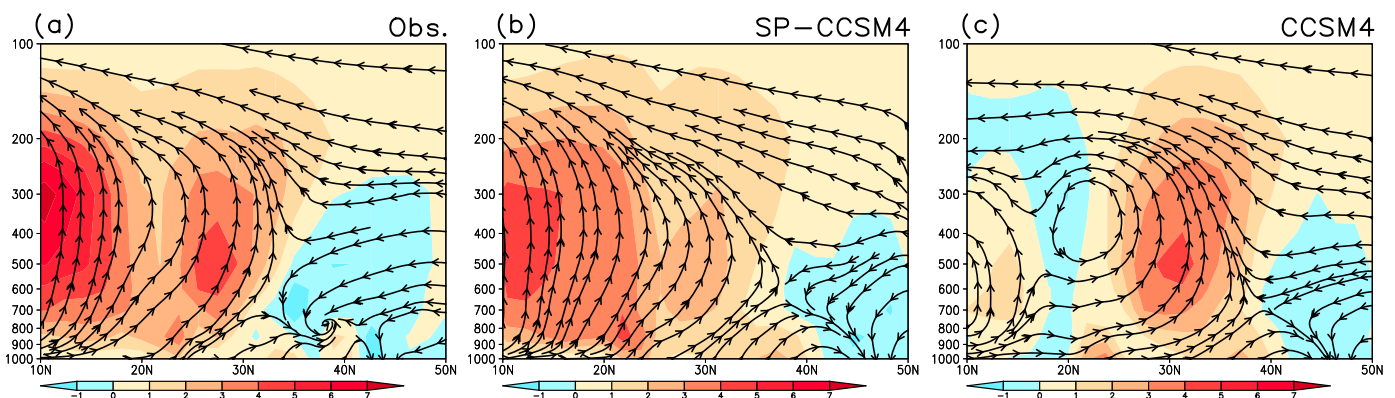


**Figure 2.** The MJJA mean GPH at 850 hPa (unit: m). (a) Observations (black), SP-CCSM4 (red) and CCSM4 (blue), (b) the difference between SP-CCSM4 and observations, and (c) the difference between CCSM4 and observations. In Figure 2a the solid contours are the isopleths of 1500 m and the dashed lines denote the ridge line of WNP SH. The dots in Figures 2b and 2c denote regions exceeding 95% significance level. The values at the top-left and top-right corners of Figures 2b and 2c have the same meaning as in Figure 1, except for the 850 hPa GPH.

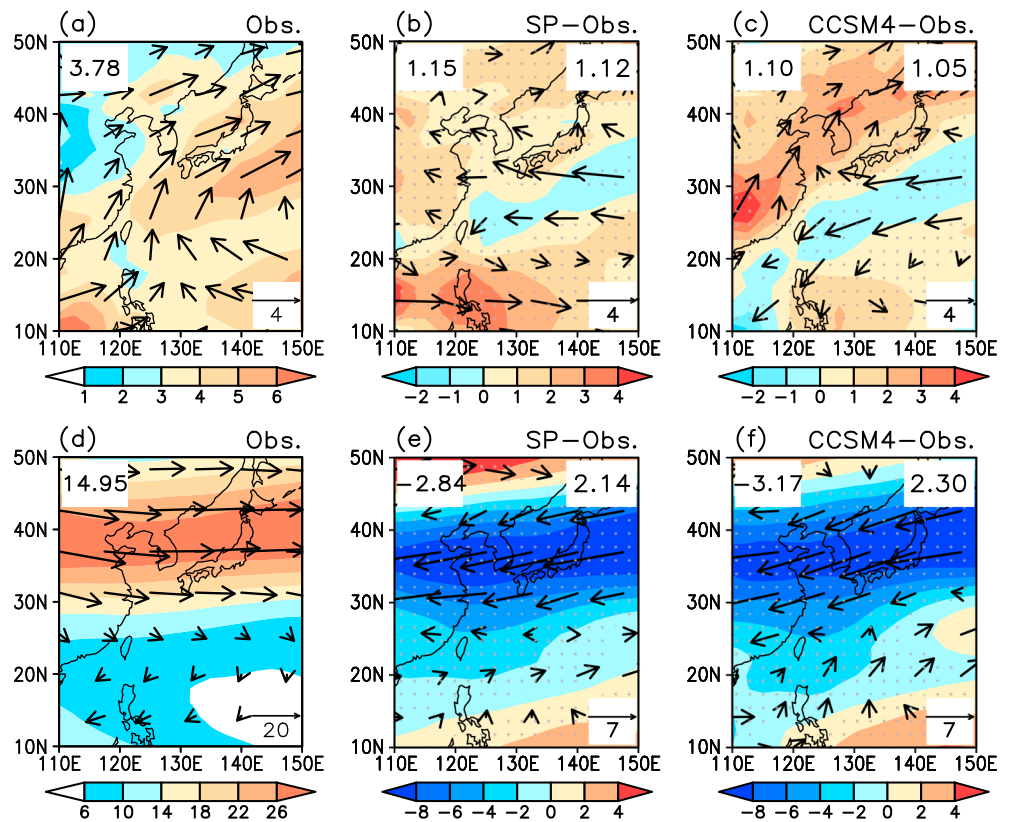
Figures 2b and 2c. In observations the western edge of the 1500 m isopleth reaches 130°E, and the ridge line is located between 20°N and 30°N. Compared to observations, the WNP SH in SP-CCSM4 is displaced northward (Figure 2a) and is weaker (Figure 2b). The western edge of 1500 m isopleth retreats to 140°E; the ridge line stays at approximately 30°N over the Pacific Ocean and tilts northward as it approaches the East Asia continent. This northward shift of WNP SH relative to observations was also found in AOGCMs [Kusunoki and Arakawa, 2015] and AGCMs [Song and Zhou, 2014; He and Zhou, 2014] of CMIP5. In CCSM4 the WNP SH expands northwestward; the 1500 m isopleth extends to the west of 120°E. The lower domain-averaged difference of 850 hPa GPH indicates that the WNP SH is better simulated in SP-CCSM4 than in CCSM4.

Figure 3 depicts the MJJA mean meridional circulation averaged between 110°E and 120°E in observation, SP-CCSM4, and CCSM4, respectively. Both models reproduce the observed centers of maximum ascending motion: one center is located between 10°N and 20°N, and the other one to its north. However, there are noticeable biases in both models. In SP-CCSM4 the rising motion between 25°N and 35°N is weaker than in observations, which is consistent with the precipitation deficiency over the eastern coast of China (Figure 1b). In CCSM4 the magnitude of the ascending branch to the south of 20°N is underestimated, plus the upward motion at around 30°N is displaced northward compared to observations. The bias in the ascending branch is related to the intensified precipitation over central China in CCSM4 (Figure 1c).

In observations, the horizontal distribution of the low-level circulation consists of a southwesterly flow over the southern SCS, East Asia, and WNP, and a southeasterly flow over the subtropical west Pacific Ocean (Figure 4a). In SP-CCSM4 the westerly flow is overestimated over SCS and the zonal wind is reduced over the region from 20°N to 40°N. CCSM4 is characterized by stronger easterly wind over WNP as well as intensified southwesterlies over eastern China to Korean Peninsula. The lower level wind pattern is consistent with



**Figure 3.** The MJJA mean streamlines of meridional and vertical velocity averaged between 110°E and 120°E. (a) Observations, (b) SP-CCSM4, and (c) CCSM4. The shadings represent the magnitude of the vertical velocity ( $\times 10^{-2} \text{ Pa s}^{-1}$ ). The yellow-red color represents the ascending motion, and the blue color denotes the descending motion.



**Figure 4.** MJA mean wind at (a–c) 850 hPa and (d–f) 200 hPa (unit:  $\text{m s}^{-1}$ ). The shading denotes wind magnitudes, and the vectors are wind directions. Observation (Figures 4a and 4d), the difference between SP-CCSM4 and observation (Figures 4b and 4e), and the difference between CCSM4 and observation (Figures 4c and 4f). The dots in Figures 4b, 4c, 4e, and 4f denote the regions where the wind magnitude exceeds 95% significance level. The value at the top-left corner denotes the domain-averaged wind magnitudes in observation (Figures 4a and 4d) and the domain-averaged wind difference between model and observation (Figures 4b, 4c, 4e, and 4f). The value at the top-right corner of Figures 4b, 4c, 4e, and 4f denotes the domain-averaged root mean square of wind difference between model and observations.

the position and spatial distribution of WNPSH (Figure 2a). At upper levels the South Asian High (SAH) is the most prominent feature over the African-Asian region in boreal summer. Over the EASM region, the westerly jet to the northern side of SAH is underestimated in both models (Figures 4e and 4f). The domain-averaged wind difference at lower and upper levels is comparable in the two models (Figures 4b and 4c and Figures 4e and 4f), whereas the spatial pattern correlation coefficients are generally higher in SP-CCSM4.

The simulation of the thermodynamic surface fluxes is shown in Figures 5a–5c for the sensible heat flux and Figures 5d–5f for the latent heat flux. In both models the sensible heat flux is overestimated approximately between 20°N and 32°N and underestimated to the north of this region. Aside from the sensible heat flux, the latent heat flux over the central and eastern China is underestimated in SP-CCSM4 while is overestimated in CCSM4 (Figures 5e and 5f). Therefore, over eastern China, CCSM4 simulates moist conditions and SP-CCSM4 simulates dry conditions.

The moisture transport into the monsoon region is known to influence the precipitation. In observations, the moisture transport from SCS splits into a branch that turns northward, merging with the moisture transport from WNP (Figure 6a). As mentioned above, the moisture transport is associated with the spatial distribution of WNPSH. In SP-CCSM4 the WNPSH is displaced northeastward (red contour in Figure 2a); thus, the northeastward flowing moisture transport becomes weaker (Figure 6b). While in CCSM4 (blue contour in Figure 2a) the WNPSH extends westward, which induces larger amount of moisture to the western and northern sides of the EASM area (Figure 6c). Therefore, the precipitation in CCSM4 is reduced over Southeast China, Korean Peninsula, and southern Japan (Figure 1c).

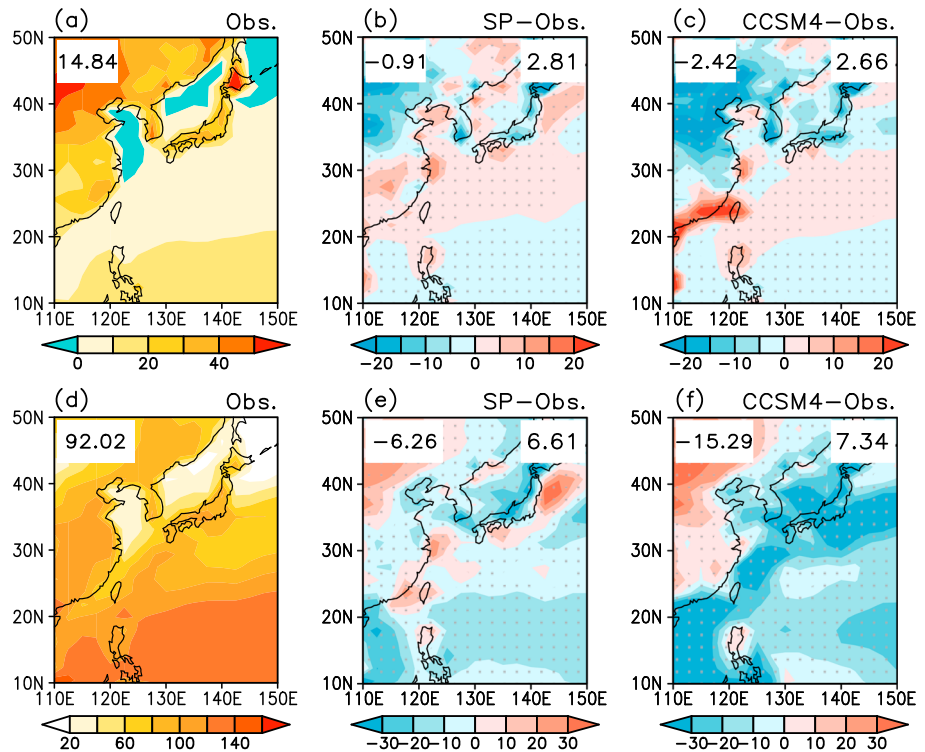


**Figure 5.** (a–c) MJJA mean sensible heat flux and (d–f) latent heat flux (unit:  $W s^{-2}$ ). Observation (Figures 5a and 5d), the difference between SP-CCSM4 and observation (Figures 5b and 5e), and the difference between CCSM4 and observation (Figures 5c and 5f). The dots in Figures 5b, 5c, 5e, and 5f denote the regions exceeding 95% significance level. The value at the top-left corner denotes the domain-averaged heat flux in observation (Figures 5a and 5d) and the domain-averaged heat flux difference between model and observation (Figures 5b, 5c, 5e, and 5f). The value at the top-right corner of Figures 5b, 5c, 5e, and 5f denotes the domain-averaged root mean square of heat flux difference between model and observations.

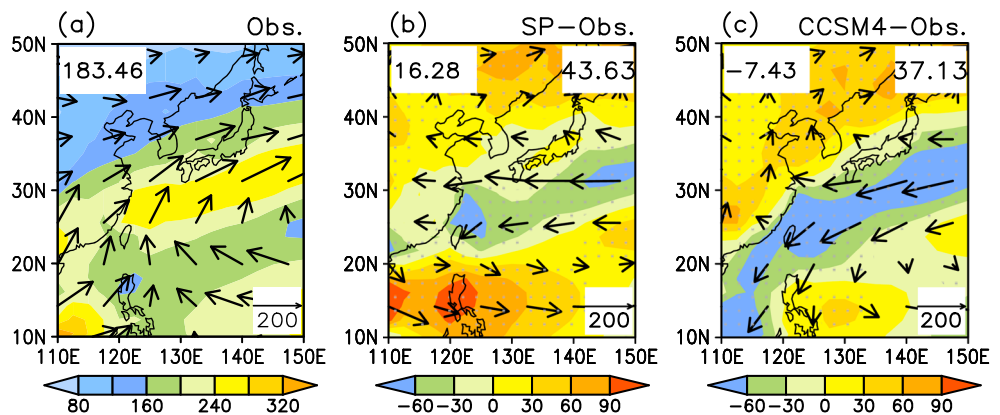


**Figure 6.** MJJA mean vertically integrated moisture transport (unit:  $Kg m^{-1} s^{-1}$ ). The shading represents magnitudes of moisture transport, and the vectors denote directions. (a) Observations, (b) the difference between SP-CCSM4 and observations, and (c) the difference between CCSM4 and observations. The dots in Figures 6b and 6c denote the regions where the difference in the magnitude of moisture transport exceeds 95% significance level. The value at the top-left corner denotes the domain-averaged magnitude of moisture transport in observations (Figure 6a) and the domain-averaged difference of moisture transport between model and observations (Figures 6b and 6c). The value at the top-right corner of Figures 6b and 6c denotes the domain-averaged root mean square of moisture transport difference between model and observations.

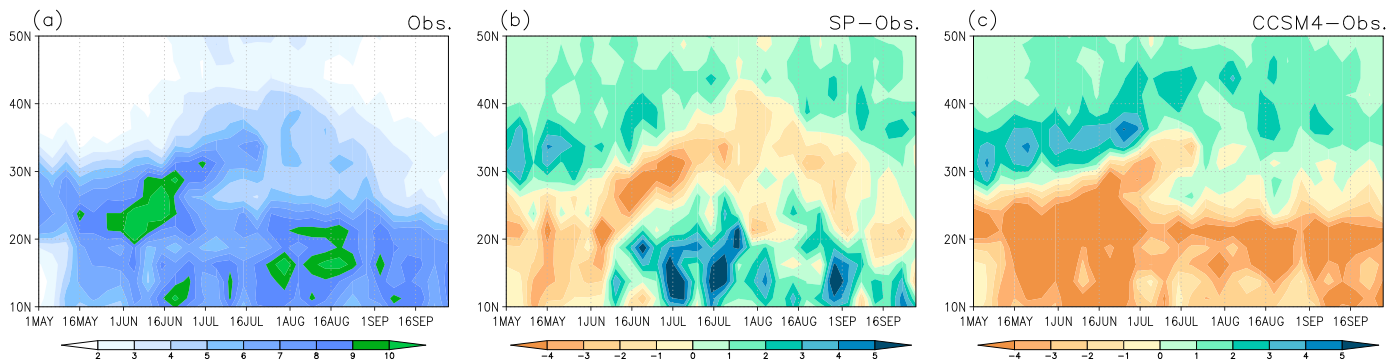


**Figure 7.** Latitude-time cross section of pentad mean precipitation rate averaged between 110°E and 120°E (unit: mm/d): (a) observations, (b) difference between SP-CCSM4 and observations, and (c) difference between CCSM4 and observations.

SP-CCSM4 has higher correlation coefficients than CCSM4 for 11 out of the 15 variables in Table 1. These comparisons suggest that SP-CCSM4 has a better skill in simulating the MJJA mean state of EASM. The analysis also reveals that both models have shortcomings in simulating the observed features of EASM. The models' biases in simulating the precipitation field are largely due to the position and magnitude of the WNPSH, which influence the low-level wind and moisture transport.

### 3.2. Annual Cycle of EASM

The annual cycle of EASM of each model is compared to observations. The time series at each grid point is constructed using climatological pentad mean data. Figure 7 shows the annual cycle of the zonal mean precipitation averaged between 110°E and 120°E. In observations, after the first 10 days of May, the equatorial rain belt propagates northward rapidly and merges with the rain belt over South China, leading to an increase of precipitation there. This rainy episode corresponds to the first standing stage of the EASM seasonal march. Before mid-May the rainband located between 20°N and 28°N is called the presummer rainy season in South China [Ding and Chan, 2005]. Around 10 June the rain belt shifts northward and stays between 28°N and 32°N until early July. This rainy episode represents the Mei-yu season and is also referred to as the second standing stage of the EASM seasonal march. Afterwards, it advances northward again reaching to North China (Figure 7a). The seasonal march of the EASM rainfall described here has been documented by Ding *et al.* [2005] and Ding and Chan [2005]. Compared to the observations, SP-CCSM4 simulates the sudden northward jump of the tropical rain belt and its merger with the South China rain belt, as well as the stepwise march of the precipitation (figure not shown). However, one can notice some differences between SP-CCSM4 and observations (Figure 7b). In SP-CCSM4, the presummer rainy season over South China moves northward and the emergence of the two rain belts in mid-May is slower than in the observations (figure not shown). The subtropical branch is less intense than in the observations, while the tropical rainband is overestimated (Figure 7b). The Mei-yu season commences earlier (approximately 1 June) and spans a shorter time period in SP-CCSM4, because it lasts only until around 20 June. Also, for the last rainy period the rain belt starts to shift in late June and reaches a higher latitude than in observations. The bias in time and location leads to the rain deficiency over the EASM region in the model (Figure 7b). This deficiency in the seasonal march of the Mei-yu season is also common to CMIP5 AOGCMs [Kusunoki and Arakawa, 2015]. In CCSM4 the tropical rainband is largely underestimated throughout the whole summer (Figure 7c). The large decrease of precipitation between 10°N and 20°N in early summer implies that the merger between the tropical and subtropical rainbands at mid-May is not captured by the model; thus, the monsoon onset is simulated deficiently in CCSM4. In addition, the subtropical rainband is displaced northward (Figure 7c).

The annual cycle of the wind and vorticity at 850 hPa are also characterized by the northward propagation (Figures 8a–8c), which is consistent with the precipitation belt movement seen in Figure 7. In observations (Figure 8a), in mid-May the prevailing winds between 10°N and 20°N turn from southeasterlies to southwesterlies, indicating the onset of the SCS monsoon. One branch of the southwesterly flow shifts in steps toward the north over East Asia, while another branch remains in the subtropical region. The northward propagation is also reflected in the migration of the low-level cyclonic vorticity. SP-CCSM4 simulates the wind reversal in

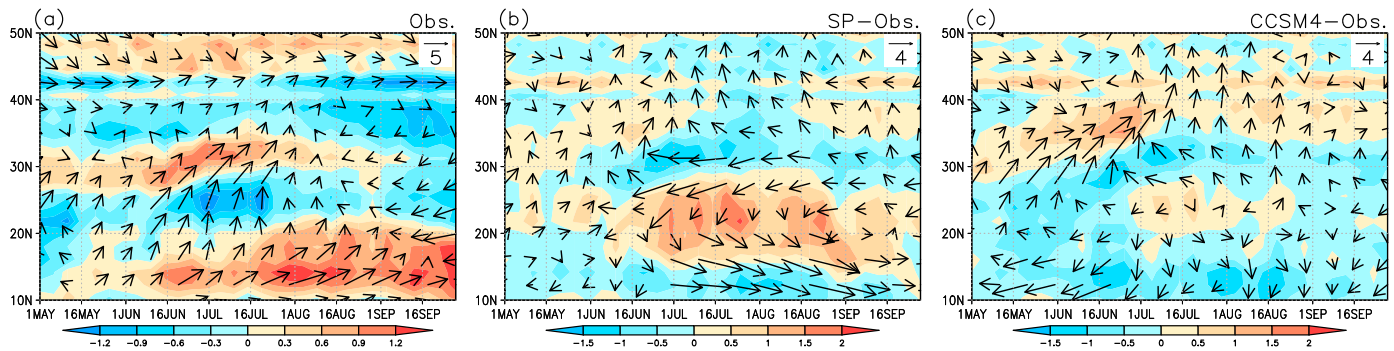


**Figure 8.** Latitude-time cross section of pentad mean 850 hPa vorticity (shading, unit:  $10^{-5} s^{-1}$ ) and 850 hPa wind (vectors, unit:  $m s^{-1}$ ) between  $110^{\circ}E$  and  $120^{\circ}E$  (unit: mm/d): (a) observations, (b) difference between SP-CCSM4 and observations, and (c) difference between CCSM4 and observations.

the subtropics in mid-May, as well as the southern branch of the southwesterly flow in the subtropics. Compared to the observations, in SP-CCSM4 the southwesterly flow and cyclonic vorticity over subtropics move northward (Figure 8b), consistent with the northward shift in the position of WNPSH. However, the southwesterly flow and the cyclonic vorticity are weaker over the EASM region starting from mid-June. This feature is consistent with the deficient rainfall and shorter period of the Mei-yu season in SP-CCSM4 (Figure 7b). In CCSM4 easterly anomalies persist over  $10^{\circ}N$ – $20^{\circ}N$  around mid-May (Figure 8c), which means that easterlies do not switch to westerlies there. This persistence indicates a delayed onset of SCS monsoon in CCSM4. In addition, in CCSM4 the northward propagation of cyclonic vorticity over the EASM domain is displaced northward compared to observations, which is associated with the northward displacement of the subtropical rainband (Figure 7c).

The difference in the annual cycle of precipitation between the models and observations can be partly explained by the migration of WNPSH, because the propagation of the rain belt is related to the meridional displacement of the WNPSH ridge line. The position of the WNPSH can be described by the index of WNPSH of Zhang and Tao [1999] applied to the GPH at 850 hPa (Figure 9). The index indicates the latitude where the 850 hPa zonal wind between  $115$  and  $140^{\circ}E$  is zero. In observations the WNPSH starts shifting northward from mid-May and reaches the northernmost position in August. In SP-CCSM4, the WNPSH starts to jump northward in early June and reaches  $40^{\circ}N$  around mid-August, which is far more northward compared to observations. In CCSM4, the WNPSH moves northward gradually from May to early June and also reaches the northernmost position in August. The WNPSH in CCSM4 is also displaced northward compared to observations.

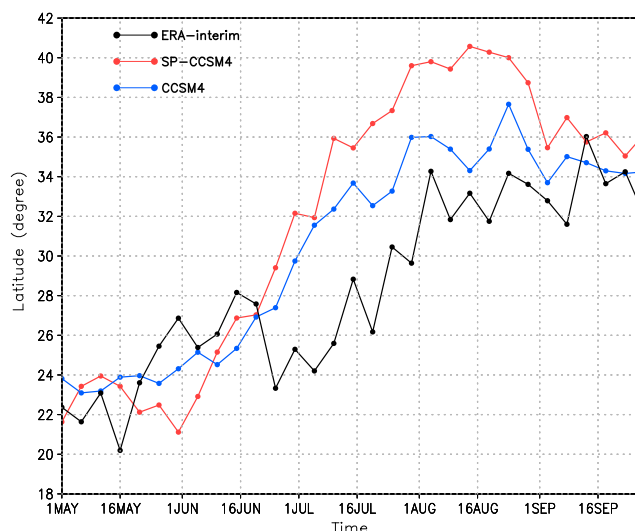


**Figure 9.** WNPSH index based on the pentad mean GPH at 850 hPa from ERA-Interim (black), SP-CCSM4 (red), and CCSM4 (blue).

The WNPSH in CCSM4 is also displaced northward compared to observations.

### 3.3. Intraseasonal Variability

To compare the 30–60 day oscillation in the model and observations, a composite analysis is applied from 15 days before to 40 days after the maximum convection occurs in SCS. The composite analysis is based on the OLR index described in the Method section. The pattern of the large OLR variance over SCS and the west Pacific is well simulated in SP-CCSM4 (Figures 10a and 10b), but the OLR variance is larger in SP-CCSM4 than in observations (Figure 10b). Here one can also speculate that periodicity and

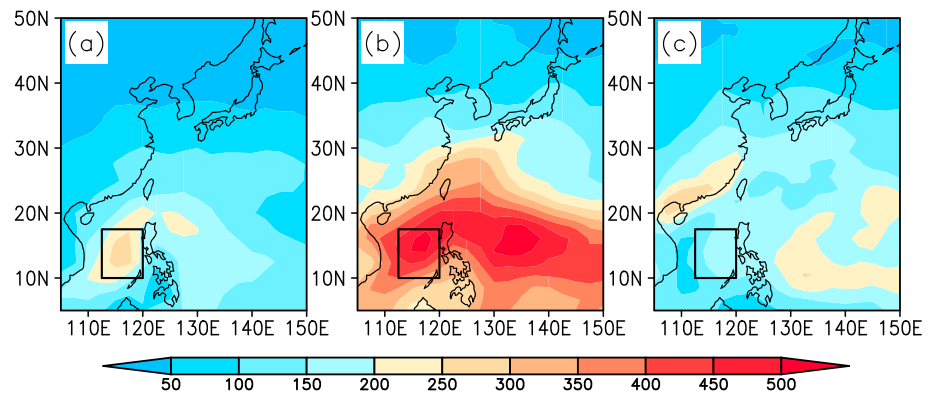


**Figure 10.** Variance of the 30–60 day bandfiltered OLR daily anomaly during MJJ (unit:  $W^2 m^{-4}$ ): (a) observation, (b) SP-CCSM4, and (c) CCSM4. The black box ( $112.5\text{--}120^\circ\text{E}$ ,  $10\text{--}17.5^\circ\text{N}$ ) is the region where the OLR variance reaches maximum in the observations.

geometry of the CRM domain artificially enhance the variability. The maximum OLR variance in SCS present in observations is not captured by CCSM4 (Figure 10c). Despite the fact that variance of the SP-CCSM4 model is larger than observed, this result suggests that intraseasonal variability is sensitive to the representation of cloud processes. The OLR index is the area-averaged OLR, where the OLR variance reaches maximum in the observation (black box in Figure 10a;  $112.5\text{--}120^\circ\text{E}$ ,  $10\text{--}17.5^\circ\text{N}$ ). This area is unchanged when we computed the OLR index for the models.

Figure 11 shows the ISO life cycle in the 30–60 day filtered OLR and 850 hPa wind field for the observations, SP-CCSM4, and CCSM4. Only the spatial patterns from day  $-15$  to day  $25$  are shown. Because the spatial pattern from day  $30$  to day  $40$  is almost the same as that from day  $-10$  to day  $0$ . From day  $-15$  to day  $-5$ , both observations and models show that convection over the tropical western Pacific develops and moves northwestward. In SP-CCSM4 the convective anomaly is more intense and extends further into the tropical and subtropical western Pacific. The convection starts moving northward/northwestward from day  $-15$  in SP-CCSM4, while in the observation, the tropical convection does not propagate northwestward until day  $-10$  when it moves eastward into the equatorial western Pacific. Therefore, the life cycle of the 30–60 day oscillation is advanced by 5 days in SP-CCSM4. In CCSM4 the convective anomaly is much weaker compared to observations (Figure 11c). It moves northwestward from tropical west Pacific Ocean into SCS from day  $-15$  to day  $-5$ .

In SP-CCSM4, between day  $-15$  and day  $-10$ , when the convection is intensified and moves to the tropical western Pacific, a westerly anomaly is located in the center and to the south of the convective region, and an easterly anomaly forms to its north. As noted in previous studies [e.g., Hsu and Weng, 2001; Kemball-Cook and Wang, 2001; Mao et al., 2010] such a flow pattern is consistent with a Gill-type Rossby wave generated by an off-equatorial heating source [Gill, 1980]. However, the easterly anomaly, which represents the Kelvin wave to the east of the convection, is not significant after day  $-5$ . The accelerated northwestward propagation of the convection starts at around day  $-15$  in SP-CCSM4, while in the observation it begins at day  $-10$ . In CCSM4 there are similar features in wind anomalies: cyclonic anomalies to the north of the convective center (Figure 11c). These cyclonic anomalies are mostly over SCS in CCSM4.

The convection in both observations and the models reaches the peak intensity in SCS and extends to the subtropical WNP at day  $0$ . In SP-CCSM4 (Figure 11b), the convection located in the subtropical WNP is stronger and tilts northward compared to observations. The tilting can be favored by the suppressed convection that SP-CCSM4 tends to produce over the West Pacific Warm Pool (WPWP). This suppressed convection appears rapidly during day  $-5$  and day  $0$ . Afterwards, it amplifies and propagates northwestward. Meanwhile in the IO, the suppressed convection propagates westward. In the observation (Figure 11a), the suppressed convection in WPWP originates from the IO and propagates eastward. Thus, the Rossby wave is more prominent in SP-CCSM4 (Figure 11b). In CCSM4 (Figure 11c) the magnitude of OLR anomalies and wind anomalies is smaller than observations and SP-CCSM4. Meanwhile, in CCSM4 there is no suppressed convection over WPWP as we see in SP-CCSM4. After day  $0$  the convection in SCS continues to move northwestward and starts dissipating in both the models and observations.

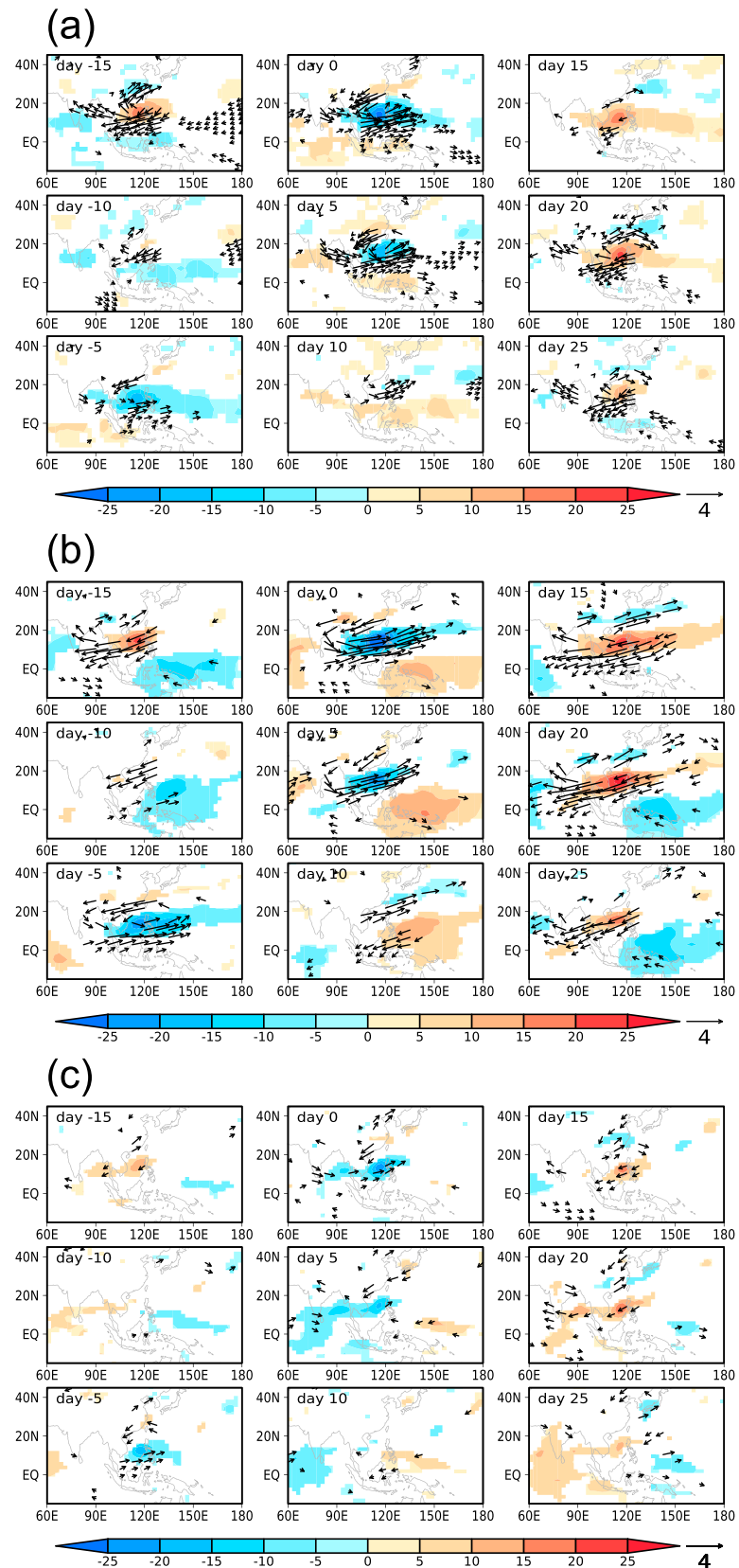


**Figure 11.** Composite of OLR (shading, unit:  $\text{Wm}^{-2}$ ) and 850 hPa wind (vectors, unit:  $\text{m s}^{-1}$ ) of the 9 ISO EASM phases, from day -15 to day 25: (a) observation, (b) SP-CCSM4, and (c) CCSM4. Only areas above 95% significance level are plotted.

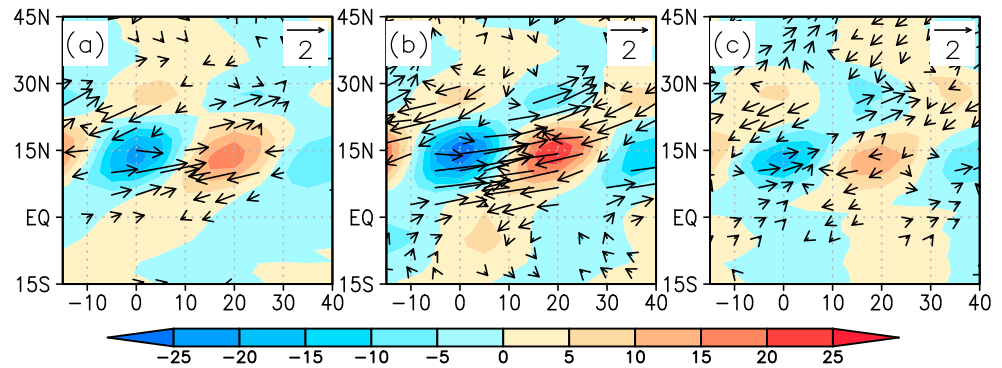


**Figure 12.** Zonally averaged ( $110\text{--}120^\circ\text{E}$ ) 12 phases of the ISO EASM in OLR (shading, unit:  $\text{Wm}^{-2}$ ) and 850 hPa wind (vectors, unit:  $\text{m s}^{-1}$ ) for (a) observations, (b) SP-CCSM4, and (c) CCSM4. The wind magnitude smaller than  $0.1 \text{ m s}^{-1}$  is not plotted.

From day +5 to day +10, the dipole pattern of the active and suppressed convection over SCS and WNP has a northwest-southeast tilt in SP-CCSM4 (Figure 11b), while in the observations (Figure 11a) the pattern is aligned in the north-south direction. The active and suppressed convection are both stronger in SP-CCSM4. Moreover, the region of suppressed convection to the north of the convectively active center dissipates rapidly in SP-CCSM4, whereas in the observation the suppressed convection persists to the north and east of the convectively active region until day +15. It appears that the shrinkage of the region with suppressed convection favors the faster northward propagation of convection in SP-CCSM4. In CCSM4 (Figure 11c) the suppressed convective activity over the tropical west Pacific moves westward from day +5; at the same time, the convective activity over SCS dissipates rapidly.

In SP-CCSM4 (Figure 11b) at day +15, the convection over SCS moves northward into Southeast China. Meanwhile, the northeasterly anomaly at  $30^\circ\text{N}$  starts to turn into southwesterly anomaly, initiating the Mei-yu season. The Mei-yu season lasts until about day +25. In the observations (Figure 11a), the southwesterly flow and the convection start to develop over Southeast China at around day +20. In CCSM4 (Figure 11c) southwesterly anomalies and negative OLR anomalies over Southeast China persist from day +20 to day +25.

The northward propagation of the active and break precipitation phases of the EASM can be seen more clearly from the zonally averaged OLR and 850 hPa wind between  $110$  and  $120^\circ\text{E}$  during day  $-15$  to day  $40$  (Figures 12a–12c). In SP-CCSM4 (Figure 12b) before the Mei-yu onset, the region with suppressed convection to the north of the convectively active center disappears quickly, favoring the convection to move further northward. Meanwhile, the convective activity at around  $15^\circ\text{N}$  propagates northward and moves to the Mei-yu region (around  $30^\circ\text{N}$ ) fast. Therefore, in SP-CCSM4, the Mei-yu season starts 5 days earlier and lasts for a shorter time period (10 days) than in observations (15 days). The similar feature can be seen in CCSM4 (Figure 12c). The suppressed convection over  $30^\circ\text{N}$  at day 0 does not persist as long as that in observations (Figure 12a), thus favoring the northward propagation of the convective anomalies.

The mechanisms proposed to explain the northward propagation of the EASM are investigated in an attempt to understand which mechanism is deficient in the models. Figure 13 shows the spatial pattern of the ISO life cycle (from day  $-15$  to day 25) of surface temperature superposed with OLR in observations and models. Before day 0, a warm SST anomaly is located to the northern side of the region with active convection, leading the convection to propagate northward from the Maritime Continent to SCS (Figure 13a). This feature is also presented in SP-CCSM4 and CCSM4 (Figures 13b and 13c). In observations, the maximum convection over SCS is followed by a warming of SST to the south of Japan and over the Maritime Continent, and a cooling of SST in between. This cold SST leads the suppressed convection over the Maritime Continent and induces its northward propagation to SCS. At the same time, the warmer SST to the south of Japan makes the convection move northeastward. The main difference between SP-CCSM4 and observation appears after day 0 when in SP-CCSM4 negative SST anomalies form to the south of Japan. The cold SSTs to the south of Japan do not favor the northeastward propagation of convection. In CCSM4 (Figure 13c) there are positive SST anomalies to the south of Japan while negative surface temperature anomalies over East China. Combining with the life cycle of the low-level wind pattern (Figure 11), SP-CCSM4 reproduces the air-sea interaction mechanism

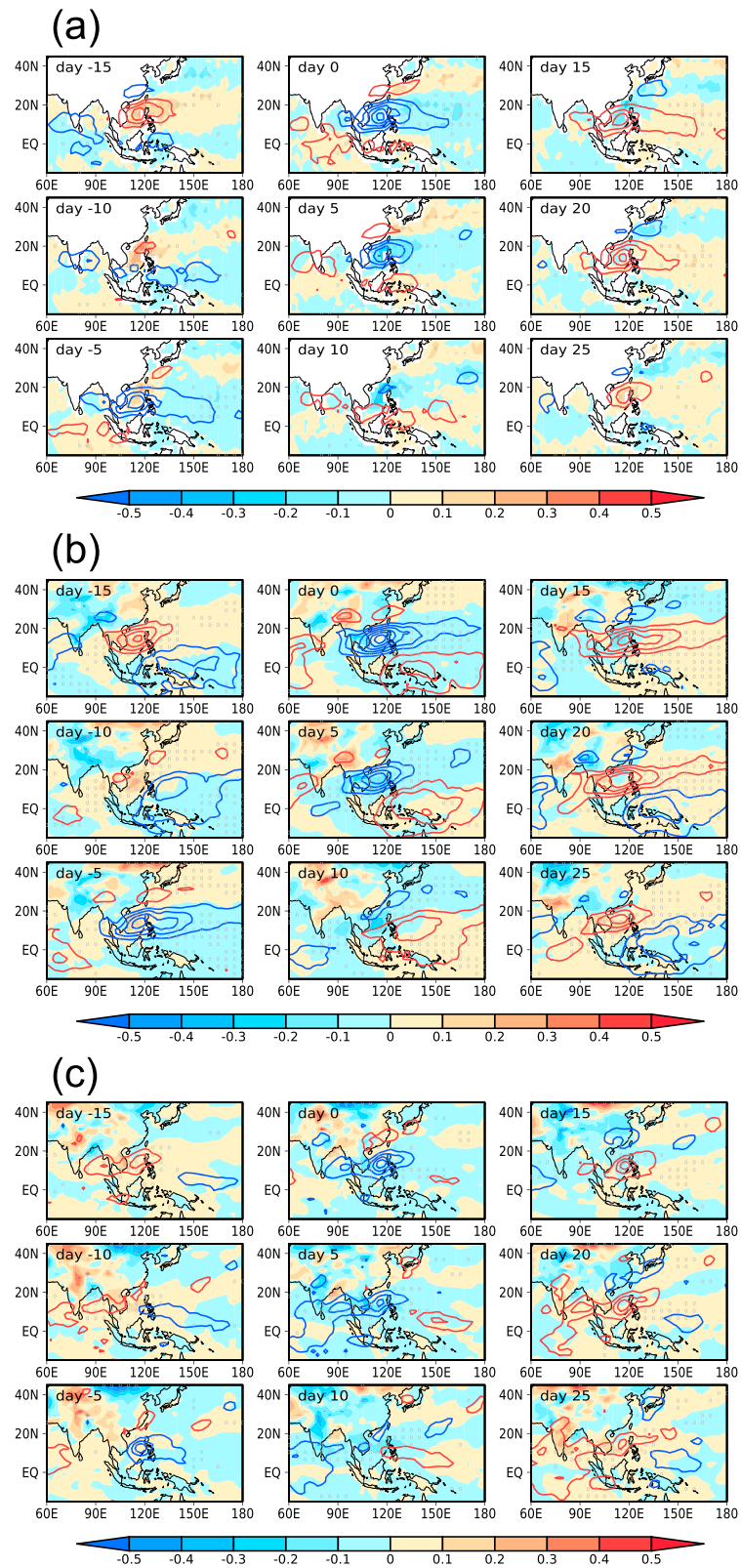


**Figure 13.** Composite of surface temperature (shading, unit: K) and OLR (contours, unit:  $Wm^{-2}$ ) of the 9 ISO EASM phases, from day  $-15$  to day  $25$ : The blue contours denote convective anomalies, and the red contours represent suppressed convective anomalies. The contour interval is  $5 Wm^{-2}$ , and the minimum (maximum) value for convective (suppressed convective) anomalies is  $5 (-5) Wm^{-2}$ . The dots indicate the areas where the composite SST is above 95% significance level.

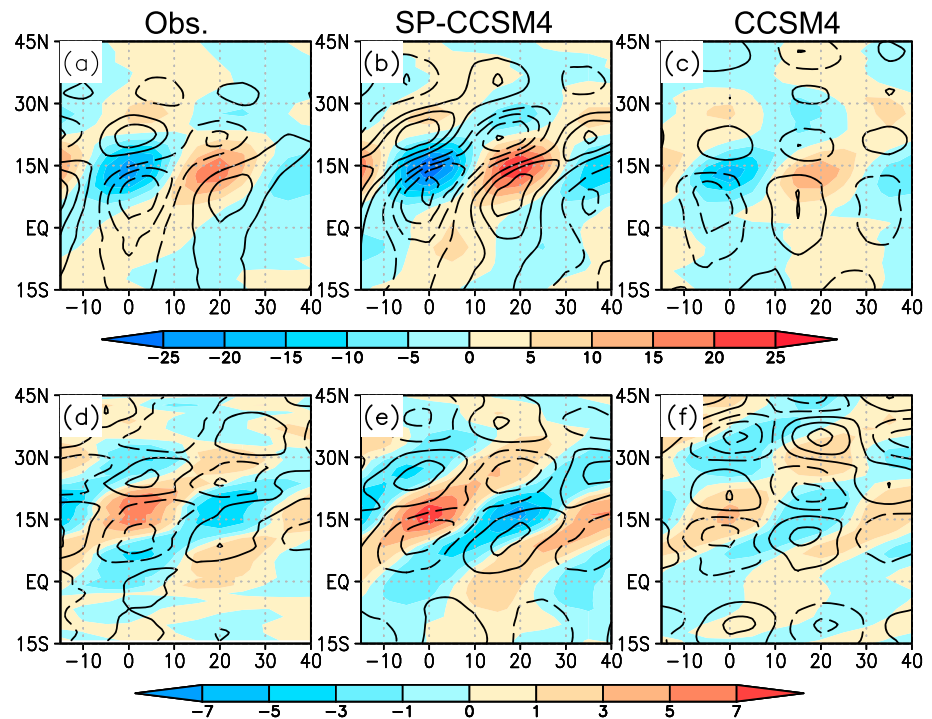


**Figure 14.** (a–c) Zonally averaged (110°E–120°E) OLR (shading, unit:  $\text{Wm}^{-2}$ ) and vertical wind shear based on the difference between the zonal wind at 200 hPa and 850 hPa (contours, unit:  $\text{m s}^{-1}$ ). (d–f) Zonally averaged 850 hPa vorticity (shading, unit:  $10^{-6} \text{ s}^{-1}$ ) and 200 hPa vorticity (contours, unit:  $10^{-6} \text{ s}^{-1}$ ). Observations (Figures 14a and 14d), SP-CCSM4 (Figures 14b and 14e), and CCSM4 (Figures 14c and 14f). In Figures 14a–14c the solid contours denote westerly wind shear, and the dashed contours denote easterly wind shear. The contour interval is  $1 \text{ m s}^{-1}$ . In Figures 14d–14f the solid contours denote the cyclonic vorticity at 200 hPa, and the dashed contours denote the anticyclonic vorticity at 200 hPa. The contour interval is  $10^{-6} \text{ s}^{-1}$ .

favoring the northward propagation of the ISO. The convection (suppressed convection) induces a cyclonic (anticyclonic) circulation anomaly to its northwestern side. The northeasterly (southwesterly) anomaly to the north of the convection reduces (enhances) the prevailing southwesterly flow, and thus decreases (increases) the upward latent heat flux. The variation in latent heat flux results in the warming (cooling) of SST to the north of convection (suppressed convection), which increases (decreases) the convective instability, thus favoring the northward movement of convection (suppressed convection).

Both the models and observations (Figure 14) show that before the onset of the Mei-yu season over Southeast China (day +20 in the observations and +15 in the models), easterly wind shear prevails to the south of the convection center (Figures 14a–14c). This easterly wind shear is accompanied by barotropic vorticity to the north of convection (Figures 14d–14f), which is consistent with the vertical shear mechanism.

The patterns of circulation and convection (Figures 15b and 15c) simulated by the models are similar to observations (Figure 15a). The cyclonic (anticyclonic) vorticity leads the convection (suppressed convection), staying to the north of convection (suppressed convection) and favoring the northward propagation of the convective activity. However, in SP-CCSM4 (Figure 15b) both the cyclonic and anticyclonic vorticity are more intense than in observations (Figure 15a), while in CCSM4 (Figure 15c) the vorticity anomalies are relatively weaker than in observations. In both models (Figures 15b and 15c), the anticyclonic vorticity before day +10 propagates faster than that in observations (Figure 15a), creating conditions for the northward movement of the cyclonic vorticity.

The composite of the zonally averaged low-level moisture convergence (Figures 15d–15f) shows a similar pattern to the vorticity field. SP-CCSM4 (Figure 15e) simulates a stronger moisture convergence (divergence) compared to observations (Figure 15d), whereas in CCSM4 (Figure 15f) the magnitude of moisture convergence is comparable to observations. Meanwhile, the moisture convergence (divergence) is located slightly to the north of convective (suppressed convection) center, which is similar to observation. The cyclonic

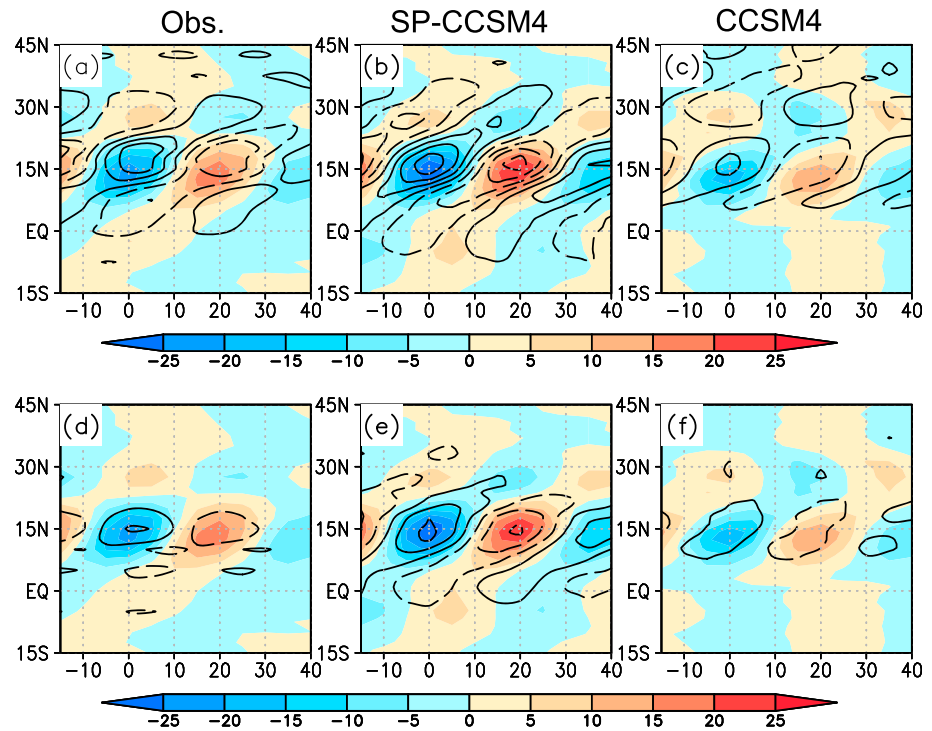


**Figure 15.** Same as Figure 14 but (ac) for the zonally averaged (110°E–120°E) OLR (shading, unit:  $\text{Wm}^{-2}$ ) and 850 hPa vorticity (contours, unit:  $10^{-6} \text{ s}^{-1}$ ), (d–f) the zonally averaged OLR (shading, unit:  $\text{Wm}^{-2}$ ), and 1000 hPa moisture convergence (contours, unit:  $10^{-8} \text{ s}^{-1}$ ). Observations (Figures 15a and 15d), SP-CCSM4 (Figures 15b and 15e), and CCSM4 (Figures 15c and 15f). In Figures 15a–15c the solid contours denote cyclonic vorticity, and the dashed contours denote anti cyclonic vorticity. The contour interval is  $2 \times 10^{-6} \text{ s}^{-1}$ . In Figures 15d–15f the solid contours denote moisture convergence, and the dashed contours denote moisture divergence. The contour interval is  $2 \times 10^{-8} \text{ s}^{-1}$ .

vorticity and moisture convergence to the north of the convection also tend to destabilize the atmospheric boundary layer, thus driving the convection to move northward.

#### 4. Summary and Discussions

The ability of SP-CCSM4 and CCSM4 to simulate the observed features of EASM is evaluated by comparing the model output with observations. The comparisons include the MJJA mean state, the annual cycle, and the ISO associated with the EASM variability. The models capture the main features of the EASM observed climatology and the mechanisms related to its northward propagation.

The MJJA mean state of EASM is better simulated by SP-CCSM4 than CCSM4. Both models underestimate the amount of precipitation over the EASM area. In SP-CCSM4 the rainfall deficiency results from a combination of factors including a northward displaced WNPSH and less moisture transport over the EASM region. In CCSM4 the WNPSH extends westward, favoring the intrusion of moisture to central and northeastern China as well as northern Japan.

The SP-CCSM4 also captures many aspects of the stepwise northward propagation of the precipitation belt in the EASM region. The shortcomings of the SP-CCSM4 model in simulating the seasonal march are the early onset and shorter duration of the Mei-yu season and the more extreme northernmost position of the subtropical rain belt. The northward expansion of the edge of the subtropical rain belt is related to the northward migration of the WNPSH ridge line simulated by SP-CCSM4. In CCSM4 the EASM onset at mid-May is not captured, and the whole rainband over subtropics is displaced northward.

The underestimation of the EASM precipitation is a common problem among the current generation of climate models [Sperber *et al.*, 2013; Zhou and Li, 2002; Chen *et al.*, 2010]. The rainfall deficiency in models is largely related to the flaws in the WNPSH simulation. In SP-CCSM4, there is a weaker low-level southerly

flow over SCS and cyclonic circulation anomalies over WNP (Figures 4a–4c), which is similar to the multimodel mean of CMIP5 and CMIP3 [Sperber *et al.*, 2013, Figure 2]. The annual cycle of EASM is better simulated by SP-CCSM4 than some other models. The SP-CCSM4 reproduces the northward propagation of the subtropical rain belt with a reasonable EASM onset, except for the bias in the Mei-yu episode and the northernmost position of the rain belt. The superparameterization shows significant improvements versus CAM3.5 with different convection schemes, where the whole subtropical rain belt is displaced northward and the monsoonal precipitation lasts longer [Chen *et al.*, 2010].

SP-CCSM4 captures the mechanisms related to the northward propagation of the EASM ISO. In boreal summer, the ISO-related convective heating over the Maritime Continent and SCS induces a low-level cyclonic anomaly to the northwestern side of the convective region. The induced northeasterly anomaly reduces the prevailing southwesterly flow. The change in the low-level wind reduces the latent heat flux, leading to a warmer SST to the north of convection. This warmer SST tends to destabilize the atmospheric boundary layer, thus favoring the northward propagation of convection. Meanwhile, the presence of the easterly vertical shear and the barotropic vorticity to the north of the convective activity also contributes to the northward propagation of ISO. The difference between the model and observation is that the northwestward propagation starting from WNP occurs earlier and moves faster in the model. In addition, the Mei-yu season begins earlier and does not last as long.

The analysis of mechanisms responsible for the northward propagation does not indicate large discrepancies between their representation in SP-CCSM4 and observations. The largest difference we notice between SP-CCSM4 and observations is a region of suppressed convection over WPWP, which is present only in SP-CCSM4 (Figure 11). This suggests that the earlier onset of the Mei-yu season and the faster northward propagation could be attributed to this region of suppressed convection. The study of the impact of WPWP condition on the EASM ISO will be presented in part II.

#### Acknowledgments

We thank all the scientists and software engineers who contributed to the development of the CCSM4 and the superparameterization. This work has been supported by the Regional and Global Climate Modeling Program funded by U.S. Department of Energy, Office of Science under award number SC0006722 and by the National Science Foundation and Technology Center for Multi-scale Modeling of Atmospheric Processes managed by Colorado State University under cooperative agreement no. ATM-0425247. This research used resources of the National Energy Research Scientific Computing Center, which is supported by the Office of Science of the U.S. Department of Energy under Contract DE-AC02-05CH11231 and the Extreme Science and Engineering Discovery Environment, which is supported by National Science Foundation grant OCI-1053575. We would like to acknowledge high-performance computing support from Yellowstone (ark:/85065/d7wd3xhc) provided by NCAR's Computational and Information Systems Laboratory, sponsored by the National Science Foundation. The authors appreciate the comments on the manuscript by V. Krishnamurthy and Nicholas Lybarger.

#### References

- Chai, T., and R. R. Draxler (2014), Root mean square error (RMSE) or mean absolute error (MAE)? – Arguments against avoiding RMSE in the literature, *Geosci. Model. Dev.*, *7*, 1247–1250.
- Chen, H., T. Zhou, R. B. Neale, X. Wu, and G. Zhang (2010), Performance of the New NCAR CAM3.5 in East Asian Summer Monsoon Simulations: Sensitivity to modifications of the convection scheme, *J. Clim.*, *23*, 3657–3675, doi:10.1175/2010JCLI3022.1.
- Dee, D. P., et al. (2011), The ERA-Interim reanalysis: Configuration and performance of the data assimilation system, *Q. J. R. Meteorol. Soc.*, *137*(656), 553–597.
- DeMott, C., C. Stan, and D. A. Randall (2013), Northward propagation mechanisms of the Boreal Summer Intraseasonal Oscillation in the ERA-Interim and SP-CCSM, *J. Clim.*, *26*, 1973–1992, doi:10.1175/JCLI-D-12-00191.1.
- Ding, Y. (1992), Summer monsoon rainfalls in China, *J. Meteorol. Soc. Japan*, *70*, 373–396.
- Ding, Y., and J. C. Chan (2005), The East Asian Summer Monsoon: An overview, *Meteorol. Atmos. Phys.*, *89*, 117–142, doi:10.1007/s00703-005-0125-z.
- Ding, Y., H. Wang, and B. Wang (2005), East Asian Monsoon: East Asia, in *The Global Monsoon System: Research and Forecast. Report of the International Committee of the Third International Workshop on Monsoons (IWM-III), Hangzhou, China*, edited by C.-P. Chang, B. Wang, and N.-C. G. Lau, pp. 95–114, Secretariat of World Meteorological Organization, Geneva, Switzerland.
- Drbohlav, H.-K. L., and B. Wang (2005), Mechanism of the Northward-Propagating Intraseasonal Oscillation: Insights from a Zonally Symmetric Model, *J. Clim.*, *18*, 952–972, doi:10.1175/JCLI3306.1.
- Gent, P. R., et al. (2011), The Community Climate Model Version 4, *J. Clim.*, *24*, 4973–4991.
- Gill, A. E. (1980), Some simple solutions for heat-induced tropical circulation, *Q. J. R. Meteorol. Soc.*, *106*, 447–462.
- Grabowski, W. W. (2001), Coupling cloud processes with the large-scale dynamics using the Cloud-Resolving Convection Parameterization (CRCP), *J. Atmos. Sci.*, *58*, 978–997.
- He, C., and T. Zhou (2014), The two interannual variability modes of the western North Pacific subtropical high simulated by 28 CMIP5-AMIP models, *Clim. Dyn.*, *43*, 2455–2469, doi:10.1007/s00382-014-2068-x.
- He, J. (2009), A review of the Asian-Pacific Monsoon, *Atmos. Ocean. Sci. Lett.*, *2*(2), 91–96.
- He, J., B. Zhou, M. Wen, and F. Li (2001), Vertical circulation structure, interannual variation features and variation mechanism of western Pacific subtropical high, *Adv. Atmos. Sci.*, *18*(4), 497–510, doi:10.1007/s00376-001-0040-2.
- He, J., J. Ju, Z. Wen, L. Junmei, and Q. Jin (2007), A review of recent advances in research on Asian monsoon in China, *Adv. Atmos. Sci.*, *24*(6), 972–992.
- Hsu, H.-H., and C.-H. Weng (2001), Northwestward propagation of the intraseasonal oscillation in the western North Pacific during the boreal summer: Structure and mechanism, *J. Clim.*, *14*, 3834–3850, doi:10.1175/1520-0442(2001)014<3834:NPOTIO>2.0.CO;2.
- Huang, R., L. Zhou, and W. Chen (2003), The progresses of recent studies on the variabilities of the East Asian Monsoon and their causes, *Adv. Atmos. Sci.*, *20*(1), 55–69, doi:10.1007/BF03342050.
- Huffman, G. J., R. F. Adler, P. Arkin, A. Chang, R. Ferraro, A. Gruber, J. Janowiak, A. McNab, B. Rudolf, and U. Schneider (1997), The Global Precipitation Climatology Project (GPCP) combined precipitation dataset, *Bull. Am. Meteorol. Soc.*, *78*(1), 5–20, doi:10.1175/1520-0477(1997)078<0005:TGPCCPG>2.0.CO;2.
- Jiang, X., T. Li, and B. Wang (2004), Structures and mechanisms of the northward propagating Boreal Summer Intraseasonal Oscillation, *J. Clim.*, *17*, 1022–1039, doi:10.1175/1520-0442(2004)017<1022:SAMOTN>2.0.CO;2.
- Kalnay, E., et al. (1996), The NCEP/NCAR 40-year Reanalysis Project, *Bull. Am. Meteorol. Soc.*, *77*(3), 437–471, doi:10.1175/1520-0477(1996)077<0437:TNYRP>2.0.CO;2.

- Kemball-Cook, S., and B. Wang (2001), Equatorial waves and air-sea interaction in the Boreal Summer Intraseasonal Oscillation, *J. Clim.*, *14*, 2923–2942, doi:10.1175/1520-0442(2001)014<2923:EWAASI>2.0.CO;2.
- Khairoutdinov, M. F., and D. A. Randall (2001), A cloud resolving model as a cloud parameterization in the NCAR Community Climate System Model: Preliminary Results, *Geophys. Res. Lett.*, *28*, 3617–3620, doi:10.1029/2001GL013552.
- Kusunoki, S., and O. Arakawa (2012), Change in the precipitation intensity of the East Asian summer monsoon projected by CMIP3 models, *Clim. Dyn.*, *38*, 2055–2072, doi:10.1007/s00382-011-1234-7.
- Kusunoki, S., and O. Arakawa (2015), Are CMIP5 models better than CMIP3 models in simulating precipitation over East Asia?, *J. Clim.*, *28*, 5601–5621, doi:10.1175/JCLI-D-14-00585.1.
- Liebmann, B., and C. A. Smith (1996), Description of a complete (interpolated) outgoing longwave radiation dataset, *Bull. Am. Meteorol. Soc.*, *77*, 1275–1277.
- Lu, R. (2001), Interannual variability of the summertime North Pacific subtropical high and its relation to atmospheric convection over the warm pool, *J. Meteorol. Soc. Japan*, *79*(3), 771–783, doi:10.2151/jmsj.79.771.
- Lu, R., and B. Dong (2001), Westward extension of North Pacific subtropical high in summer, *J. Meteorol. Soc. Japan.*, *79*(6), 1229–1241, doi:10.2151/jmsj.79.1229.
- Lu, R., Y. Li, and C.-S. Ryu (2008), Relationship between the zonal displacement of the western Pacific subtropical high and the dominant modes of low-tropospheric circulation in summer, *Prog. Nat. Sci.*, *18*(2), 161–165, doi:10.1016/j.pnsc.2007.07.009.
- Mao, J., Z. Sun, and G. Wu (2010), 20–50 day oscillation of summer Yangtze rainfall in response to intraseasonal variations in the subtropical high over the western North Pacific and South China Sea, *Clim. Dyn.*, *34*, 747–761, doi:10.1007/s00382-009-0628-2.
- Rajendran, K., A. Kitoh, and S. Yukimoto (2004), South and East Asian Summer Monsoon climate and variation in the MRI Coupled Model (MRI-CGCM2), *J. Clim.*, *17*, 763–782, doi:10.1175/1520-0442(2004)017<0763:SAEASM>2.0.CO;2.
- Randall, D. A., et al. (2007), Climate models and their evaluation, in *Climate Change 2007: The Physical Science Basis. Contribution of Working Group I to the Fourth Assessment Report of the Intergovernmental Panel on Climate Change*, edited by S. Solomon et al., Cambridge Univ. Press, Cambridge, U. K., and New York.
- Reynolds, R. W., N. A. Rayner, T. M. Smith, D. C. Stokes, and W. Wang (2002), An improved in situ and satellite SST analysis for climate, *J. Clim.*, *15*, 1609–1625, doi:10.1175/1520-0442(2002)015<1609:AISAS>2.0.CO;2.
- Song, F., and T. Zhou (2014), Interannual variability of East Asian Summer Monsoon simulated by CMIP3 and CMIP5 AGCMs: Skill dependence on Indian Ocean-western Pacific anticyclone teleconnection, *J. Clim.*, *27*, 1679–1697, doi:10.1175/JCLI-D-13-00248.1.
- Sperber, K. R., H. Annamalai, L.-S. Kang, A. Kitoh, A. Moise, A. Turner, B. Wang, and T. Zhou (2013), The Asian summer monsoon: an intercomparison of CMIP5 vs. CMIP3 simulations of the late 20th century, *Clim. Dyn.*, *41*, 2711–2744, doi:10.1007/s00382-012-1607-6.
- Stan, C., and L. Xu (2014), Climate simulations and projections with a super-parameterized climate model, *Environ. Modell. Software*, *60*, 134–152, doi:10.1016/j.envsoft.2014.06.013.
- Sun, S., and M. Ying (1999), Subtropical high anomalies over the western Pacific and its relations to the Asian monsoon and SST anomaly, *Adv. Atmos. Sci.*, *16*(4), 559–568, doi:10.1007/s00376-999-0031-2.
- Tao, S., and L. Chen (1987), A review of recent research on the East Asian Monsoon in China, in *Monsoon Meteorology*, edited by C.-P. Chang and T. N. Krishnamurti, pp. 60–92, Oxford Univ. Press, London.
- Tompkins, A. M. (2000), The impact of dimensionality on long-term cloud resolving model simulations, *Mon. Weather Rev.*, *128*, 1521–1535, doi:10.1175/1520-0493(2000)128<1521:TIODOL>2.0.CO;2.
- Tsou, C.-H., P.-C. Hsu, W.-S. Kau, and H.-H. Hsu (2005), Northward and northwestward propagation of 30–60 day oscillation in the tropical and extratropical western North Pacific, *J. Meteorol. Soc. Japan*, *83*(5), 711–726, doi:10.2151/jmsj.83.711.
- Wang, B., and Q. Zhang (2002), Pacific-East Asian teleconnection. Part II: How the Philippine Sea Anomalous Anticyclone is established during El Niño development, *J. Clim.*, *15*, 3252–3265, doi:10.1175/1520-0442(2002)015<3252:PEATPI>2.0.CO;2.
- Wang, B., R. Wu, and X. Fu (2000), Pacific-East Asian teleconnection: How does ENSO affect East Asian climate?, *J. Clim.*, *13*, 1517–1536, doi:10.1175/1520-0442(2000)013<1517:PEATHD>2.0.CO;2.
- Wang, B., T. Li, Y. Ding, R. Zhang, and H. Wang (2005), East Asian-Western North Pacific Monsoon: A distinctive component of the Asian-Australian monsoon system, in *The Global Monsoon System: Research and Forecast. Report of the International Committee of the Third International Workshop on Monsoons (IWM-III), Hangzhou, China*, edited by C.-P. Chang, B. Wang, and N.-C. G. Lau, pp. 95–114, Secretariat of World Meteorological Organization, Geneva, Switzerland.
- Wang, B., F. Huang, Z. Wu, J. Yang, X. Fu, and K. Kikuchi (2009), Multi-scale climate variability of the South China Sea monsoon: A review, *Dyn. Atmos. Oceans*, *47*(1–3), 15–37, doi:10.1016/j.dynatmoce.2008.09.004.
- Wang, S., and A. H. Sobel (2011), Response of convection to relative sea surface temperature: Cloud-resolving simulations in two and three dimensions, *J. Geophys. Res.*, *116*, D11119, doi:10.1029/2010JD015347.
- Willmott, C., and K. Matsuura (2005), Advantages of the mean absolute error (MAE) over the root mean square error (RMSE) in assessing average model performance, *Clim. Res.*, *30*, 79–82.
- Yang, H., and S. Sun (2003), Longitudinal displacement of the subtropical high in the western Pacific in summer and its influence, *Adv. Atmos. Sci.*, *20*(6), 921–933, doi:10.1007/BF02915515.
- Zeng, X., et al. (2007), Evaluating clouds in long-term cloud resolving model simulations with observational data, *J. Atmos. Sci.*, *64*, 4153–4177, doi:10.1175/2007JAS2170.1.
- Zhang, L., B. Wang, and Q. Zeng (2009), Impact of the Madden-Julian Oscillation on summer rainfall in southeast China, *J. Clim.*, *22*, 201–217, doi:10.1175/2008JCLI1959.1.
- Zhang, Q., and S. Tao (1999), The study of the sudden northward jump of the subtropical high over the western Pacific, *Acta Meteorol. Sin.*, *57*, 539–548.
- Zhou, T., et al. (2009), Why the western Pacific subtropical high has extended westward since the late 1970s, *J. Clim.*, *22*, 2199–2215, doi:10.1175/2008JCLI2527.1.
- Zhou, T.-J., and Z.-X. Li (2002), Simulation of the East Asian Summer Monsoon using a variable resolution atmospheric GCM, *Clim. Dyn.*, *19*, 166–180, doi:10.1007/s00382-001-0214-8.